

Giant optical anisotropy in transition metal dichalcogenides for next-generation photonics

Georgy Ermolaev

Moscow Institute of Physics and Technology, <https://orcid.org/0000-0002-0895-818X>

D. Grudin

Moscow Institute of Physics and Technology <https://orcid.org/0000-0003-4038-5374>

Y. Stebunov

University of Manchester

K. Voronin

Moscow Institute of Physics and Technology <https://orcid.org/0000-0002-8911-1166>

Vasyl Kravets

University of Manchester

Jiahua Duan

University of Oviedo

A. Mazitov

Moscow Institute of Physics and Technology, <https://orcid.org/0000-0002-6549-7324>

G. Tselikov

Moscow Institute of Physics and Technology <https://orcid.org/0000-0002-6664-7881>

Andrei Bylinkin

CIC NanoGUNE BRTA <https://orcid.org/0000-0001-9257-0702>

D. Yakubovsky

Moscow Institute of Physics and Technology

S. Novikov

Moscow Institute of Physics and Technology (MIPT)

Denis Baranov

Chalmers University of Technology <https://orcid.org/0000-0002-8071-1587>

Alexey Nikitin

Donostia International Physics Center (DIPC) <https://orcid.org/0000-0002-2327-0164>

Ivan Kruglov

Moscow Institute of Physics and Technology

Timur Shegai

Chalmers University of Technology <https://orcid.org/0000-0002-4266-3721>

Pablo Alonso-González

University of Oviedo <https://orcid.org/0000-0002-4597-9326>

Alexander Grigorenko

University of Manchester

Aleksey Arsenin

Moscow Institute of Physics and Technology <https://orcid.org/0000-0002-7506-4389>

Kostya Novoselov

University of Manchester <https://orcid.org/0000-0003-4972-5371>

V. Volkov (✉ volkov.vs@mipt.ru)

Moscow Institute of Physics and Technology

Article

Keywords: Giant optical anisotropy, dichalcogenides, next-generation photonics, light manipulation

Posted Date: November 2nd, 2020

DOI: <https://doi.org/10.21203/rs.3.rs-97117/v1>

License:  This work is licensed under a Creative Commons Attribution 4.0 International License.

[Read Full License](#)

Version of Record: A version of this preprint was published at Nature Communications on February 8th, 2021. See the published version at <https://doi.org/10.1038/s41467-021-21139-x>.

Giant optical anisotropy in transition metal dichalcogenides for next-generation photonics

G.A. Ermolaev^{1,2}, D.V. Grudinin¹, Y.V. Stebunov³, K.V. Voronin^{1,2}, V.G. Kravets⁴, J. Duan^{5,6}, A.B.

Mazitov^{1,7}, G.I. Tselikov¹, A. Bylinkin^{1,8}, D.I. Yakubovsky¹, S.M. Novikov¹, D.G. Baranov^{9,1}, A.Y.

Nikitin^{10,11}, I.A. Kruglov^{1,7}, T. Shegai⁹, P. Alonso-González^{5,6}, A.N. Grigorenko⁴, A.V. Arsenin^{1,12}, K.S.

Novoselov^{13,3,14}, V.S. Volkov^{1,12}*

¹Center for Photonics and 2D Materials, Moscow Institute of Physics and Technology,
Dolgoprudny 141700, Russia.

²Skolkovo Institute of Science and Technology, Moscow 121205, Russia.

³National Graphene Institute (NGI), University of Manchester, Manchester M13 9PL, UK.

⁴Department of Physics and Astronomy, University of Manchester, Manchester M13 9PL, UK.

⁵Department of Physics, University of Oviedo, Oviedo 33006, Spain.

⁶Center of Research on Nanomaterials and Nanotechnology, CINN (CSIC-Universidad de
Oviedo), El Entrego 33940, Spain.

⁷Dukhov Research Institute of Automatics (VNIIA), Moscow 127055, Russia.

⁸CIC nanoGUNE BRTA, Donostia-San Sebastián 20018, Spain.

⁹Department of Physics, Chalmers University of Technology, Göteborg 412 96, Sweden.

¹⁰Donostia International Physics Center (DIPC), Donostia-San Sebastián 20018, Spain.

¹¹IKERBASQUE, Basque Foundation for Science, Bilbao 48013, Spain.

¹²GrapheneTek, Skolkovo Innovation Center, Moscow 143026, Russia.

¹³Department of Materials Science and Engineering, National University of Singapore,
Singapore 117574, Singapore.

¹⁴Chongqing 2D Materials Institute, Liangjiang New Area, Chongqing 400714, China.

*e-mail: volkov.vs@mipt.ru

26 **ABSTRACT**

27 Large optical anisotropy observed in a broad spectral range is of paramount importance for
28 efficient light manipulation in countless devices. Although a giant anisotropy was recently
29 observed in the mid-infrared wavelength range, for visible and near-infrared spectral intervals,
30 the problem remains acute with the highest reported birefringence values of 0.8 in BaTiS₃ and h-
31 BN crystals. This inspired an intensive search for giant optical anisotropy among natural and
32 artificial materials. Here, we demonstrate that layered transition metal dichalcogenides (TMDCs)
33 provide an answer to this quest owing to their fundamental differences between intralayer strong
34 covalent bonding and weak interlayer van der Waals interaction. To do this, we carried out a
35 correlative far- and near-field characterization validated by first-principle calculations that
36 reveals an unprecedented birefringence of 1.5 in the infrared and 3 in the visible light for MoS₂.
37 Our findings demonstrate that this outstanding anisotropy allows for tackling the diffraction limit
38 enabling an avenue for on-chip next-generation photonics.

39 **INTRODUCTION**

40 Optical anisotropy plays a crucial role in light manipulation owing to birefringence
41 phenomena, namely, doubling the incoming light into two different rays (called ordinary and
42 extraordinary for uniaxial optical materials), which results in spatial and polarization separation,¹
43 through versatile optical components,²⁻⁴ including polarizers, wave plates, multilayer mirrors,
44 and phase-matching elements. Their performance primarily depends on the phase retardance (ϕ)
45 between ordinary and extraordinary rays, which is proportional to the thickness (d) of the device
46 and the birefringence (Δn) of the constituting materials. Thus, a large birefringence is highly
47 favorable and beneficial since it leads to more compact and efficient devices. Despite its great
48 importance for high-performance optics, the currently used materials such as inorganic solids
49 and liquid crystals possess a quite small birefringence with typical values below 0.4.⁵⁻⁹ Even the
50 record-holders quasi-one-dimensional BaTiS₃ and layered h-BN crystals improve this result by
51 less than twofold ($\Delta n \sim 0.8$).^{10,11} The problem is partially solved in the mid-infrared range by

52 large anisotropy in the biaxial van der Waals (vdW) crystals α -MoO₃ and α -V₂O₅.^{12,13} Still, these
53 materials become mostly isotropic in the visible and near-infrared light. Meanwhile, artificial
54 design can offer large birefringence in metamaterials and metasurfaces.¹⁴ However, its
55 widespread usage is impeded by optical losses and fabrication challenges.

56 As a result, natural materials with giant anisotropy ($\Delta n > 1$) are in high demand both for
57 scientific and industrial purposes. In this regard, transition-metal dichalcogenides (TMDCs) in a
58 bulk configuration are promising candidates because of their strongly anisotropic vdW structure,
59 which naturally leads to a large intrinsic birefringence. In particular, while MoS₂ solids adopt an
60 in-plane crystalline layered structure through strong ionic/covalent bonds between molybdenum
61 (Mo) and sulfur (S) atoms, the out-of-plane link of these layers occurs via weak vdW forces in
62 trigonal prismatic configuration¹⁵, as illustrated in Figure 1a.

63 As a consequence, a strong optical anisotropy emerges in TMDCs. A diagonal permittivity
64 tensor can describe it with two optical constants corresponding to the crystallographic *ab*-plane
65 and the *c*-axis.¹⁶ Interestingly, these anisotropic properties of TMDCs were qualitatively
66 demonstrated back in 1967 by Liang *et al.*,¹⁷ but only currently attracted significant importance
67 in experiments dealing with novel regimes of light-matter interactions^{18,19} comprising exciton-
68 polariton transport,²⁰ Zenneck surface waves,²¹ tunable modal birefringence,²² and anapole-
69 exciton polaritons.²³ Although a recent pioneering work by Hu and co-workers¹⁶ reported a
70 birefringence value of $\Delta n = 1.4$ for MoS₂ at $\lambda = 1530$ nm, the values of asymmetric dielectric
71 responses of MoS₂ in a wide wavelength interval have so far remained unknown. Most likely, it
72 stems from inherent experimental difficulties while measuring a high refractive index of
73 anisotropic materials, which we overcome here by joining together far and near-field
74 characterization techniques. The method allows us to obtain the full dielectric tensor in a wide
75 wavelength range (360 – 1700 nm) and reveals giant birefringence for MoS₂ as high as $\Delta n \sim 1.5$
76 in the infrared and $\Delta n \sim 3$ in the visible spectra. This outstandingly large optical anisotropy

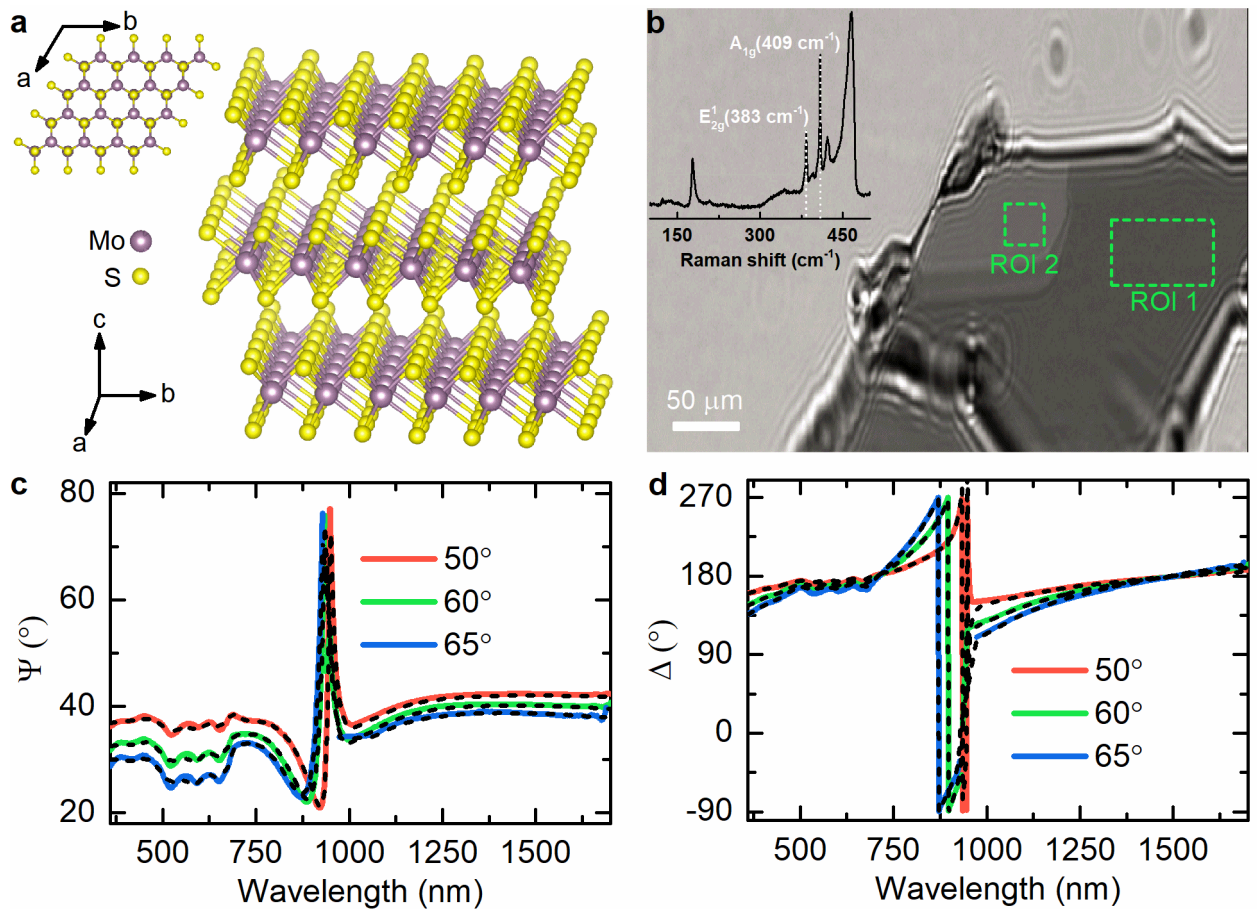
77 accompanied by a high refractive index $n \sim 4$ paves the way for highly efficient optics and light
78 manipulation in photonic chips.

79 **RESULTS**

80 The measurement of the anisotropic optical response of TMDCs is a challenging task because
81 of multiple experimental obstacles. One of the hardest parts is the implementation of traditional
82 spectroscopic diffraction-limited characterization techniques, including transmittance,
83 reflectance, and ellipsometry measurements, since bulk TMDCs are usually prepared by the
84 exfoliation method, as a result, the samples obtained have lateral dimensions of tens
85 micrometers. A second difficulty is related to the measured signal's low-sensitivity to the out-of-
86 plane components attributed to a large in-plane refractive index $n \sim 4$. For instance, in
87 ellipsometry configuration, incident light at 80° gives the refraction angle of only 14.3°
88 according to the Snell's law, which implies that the probed electric field of the refracted light
89 mainly lies along the layers and thus, is almost insensitive to the out-of-plane dielectric
90 component.

91 To overcome the latter, we prepared an exfoliated thin MoS₂ films on 285 nm SiO₂/Si
92 substrate and verified their 2H semiconducting configuration by the resonant Raman
93 demonstrated in the inset of Figure 1a since MoS₂ exists in nature in three phase modifications
94 (see details in Supporting Information): semiconducting (2H and 3R) and metallic (1T).²⁴ The
95 thick layer of silicon oxide will produce an interference-like pattern for ordinary and
96 extraordinary beams, which can readily be detected employing phase-sensitive techniques such
97 as spectroscopic ellipsometry (SE). For this reason, we performed imaging spectroscopic
98 ellipsometry (ISE) measurements in the 360 – 1700 nm wavelength range, given that it allows
99 measuring samples down to several micrometers since it is a hybrid of ellipsometer and
100 microscope (Methods). It allowed us to record the ellipsometry signal Ψ and Δ (Methods) from
101 several regions of interest (ROI) of the flakes within the selected field of view, as indicated in

102 Figure 1b. As a result, multiple sample analysis was implemented to increase data reliability (see
 103 Supporting Information). The resulting ellipsometry spectra in Figure 1c indeed shows a
 104 pronounced asymmetrical interference-like peak at around 900 nm. This is induced by a large
 105 phase difference between ordinary and extraordinary beams, indicating (without any modeling of
 106 the experimental curves) a large birefringence stemming from a strong anisotropy between the c -
 107 axis and the ab -plane.



108

109 **Figure 1. Anisotropy in MoS₂.** **a** Schematic illustration of the MoS₂ layered structure: the giant
 110 anisotropy between ab -plane and c -axis arises from different interlayer (weak van der Waals
 111 bonding) and intralayer (strong ionic/covalent bonding) atomic interactions. **b** Optical
 112 ellipsometer microscope image of the exfoliated MoS₂ thin film on a 285 nm-thick SiO₂/Si
 113 substrate at 65°. The ellipsometry measurements were performed in the two uniform areas
 114 marked by the green dashed lines. The inset shows a resonant Raman spectrum at an excitation
 115 wavelength $\lambda = 632.8$ nm with the characteristic modes $E_{2g}^1 = 383$ cm⁻¹ and $A_{1g} = 409$ cm⁻¹,

116 whose positions confirm the 2H semiconducting material configuration. **c-d** Experimental (solid
117 lines) and analytically calculated (dashed lines, see Methods) ellipsometric parameters Ψ and Δ
118 for ROI 1 (Ψ and Δ for ROI 2 see in Supporting Information) at three incident angles 50° , 60° ,
119 and 65° . The asymmetric interference-like peak at around 900 nm is induced by interference
120 enhancement in SiO_2 caused by splitting the incident beam into ordinary and extraordinary
121 beams indicating a giant anisotropy in MoS_2 .

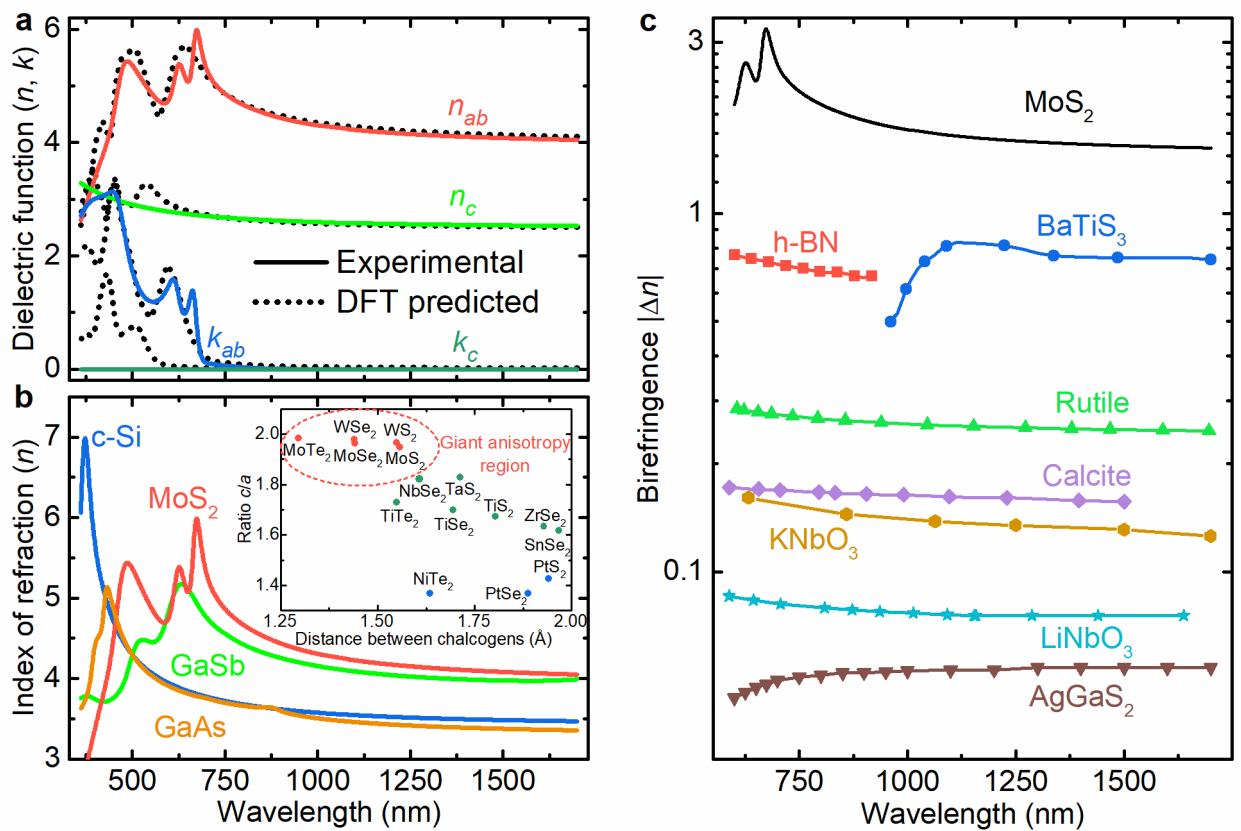
122 Notwithstanding the noticeable anisotropic feature at 900 nm in the measured spectra, to
123 accurately retrieve the complete dielectric tensor of MoS_2 and enable predictive capabilities for
124 future advanced optical devices using this material, it is imperative to develop an accurate
125 dielectric function model. In that case, the best route towards a dielectric description is to utilize
126 the crystallographic features of MoS_2 . Briefly, in its 2H structure consecutive layers are linked
127 by weak vdW forces and rotated by 180° with respect to each other leading to a strong
128 suppression of interlayer hopping for both electrons and holes, and, thus, preventing the
129 formation of tightly bound interlayer electron-hole pair upon light illumination, the so-called
130 excitons.^{25,26} Therefore, along the c -axis, the material is transparent, and a Cauchy model
131 describes its dielectric response (see Supporting Information), which is an evident consequence
132 of Kramers-Kronig relation between real (n) and imaginary (k) parts of the refractive index and
133 material transparency. In contrast, the confinement of electron and holes within the layer results
134 in enormous binding energy (~ 50 meV) for intralayer A- and B- excitons at the visible range
135 similar to its monolayer counterpart.²⁷ At the same time, it supports C and C' exciton complexes
136 at ultraviolet wavelengths due to the nest banding effects and complex atomic orbital
137 contributions.²⁸ The Tauc-Lorentz oscillator model best describes this excitonic behavior for ab -
138 plane (see Supporting Information) because it captures two the most essential physical features:²⁹
139 (i) at low photon energies, excitons cannot be excited, as a consequence, absorption, or
140 equivalently the imaginary part of refractive index (k), is equal to zero in this wavelength range

141 and (ii) excitonic peaks exhibit an asymmetric shape due to phonon coupling of bright (excited
142 by light) and dark (not excited by light) excitons.

143 Using these models for describing the optical properties of MoS₂, we fitted the experimentally
144 measured ellipsometric parameters Ψ and Δ for both ROIs at the same time (see Supporting
145 Information). The resulting ordinary (along the layers) and extraordinary (perpendicular to the
146 layers) optical constants and birefringence are displayed in Figure 2a and have a surprisingly
147 well match with the values predicted by the first-principle calculations (see Methods and
148 Supporting Information). As expected, the material along the *c*-axis is transparent, even at
149 ultraviolet and visible wavelengths. It confirms that excitons are formed in the layers and provide
150 a dichroic window from ~ 900 nm where the absorption of both ordinary and extraordinary light
151 becomes negligible. Of immediate interest is the giant birefringence of $\Delta n \sim 1.5$ in the infrared
152 and $\Delta n \sim 3$ in the visible ranges, which can serve as a platform for optical engineering in creating
153 of novel devices for the photonic application. As compared in Figure 2c, the birefringence
154 obtained for MoS₂ in the visible and near-infrared spectral intervals is several times larger than
155 for previous record-holders BaTiS₃ and h-BN,^{10,11} and an order of magnitude exceeding the
156 values of currently used birefringent materials. Particular attention should also be given to the
157 absolute values of the refractive indices, specifically their in-plane component. The high value of
158 ~ 4.1 is comparable with traditionally used isotropic high-refractive-index semiconductors,³⁰
159 including Si (~ 3.6),³¹ GaAs (~ 4.3),³² and GaSb (~ 3.9)³³ as illustrated in Figure 2b. Such a large
160 refractive index for MoS₂ opens the door for lossless subwavelength photonics with the
161 resolution of ~ 100 nm, which can easily rival with plasmonics platform, yet does not suffer from
162 losses.

163 Furthermore, as we have not specified particular properties of MoS₂ other than its in-plane
164 excitonic nature and the out-of-plane transparency, our conclusions are quite general, applying
165 equally well to other semiconductor members of layered TMDCs with hexagonal, tetragonal, and
166 trigonal atomic structure.¹ Consequently, we anticipate that other TMDCs with hexagonal

167 configuration also exhibit giant anisotropy because of the crystal's similarity. In fact, the
 168 refractive index depends upon the density of atoms in the crystal. As a consequence, naively, one
 169 could expect that the larger the distance between the layers, the higher the birefringence value
 170 between in-plane and out-of-plane dielectric response. Indeed, a comparison of their lattice
 171 parameters normalized to the distance between chalcogen intercore distances in the inset of
 172 Figure 2b explains the giant anisotropy in MoS₂ and forecasts the similar (or even higher)
 173 birefringence values for MoSe₂, WS₂, WSe₂, and WTe₂.



174
 175 **Figure 2. Optical anisotropy of MoS₂.** **a** Real (n) and imaginary (k) parts of the dielectric
 176 function along the ab -plane and c -axis. **b** Comparison of the MoS₂ refractive index along the ab -
 177 plane with other high-refractive-index materials commonly used in nanophotonics.^{31–33} The inset
 178 compares the ratio of crystal parameters (c and a in Figure 1a) versus distance between
 179 neighboring chalcogens (S, Se, and Te) for various TMDCs. The highest anisotropy is expected
 180 for TMDCs denoted by red circles, while the lowest for blue. The crystallographic data were
 181 adopted from the review article.³⁴ **c** Comparison of the absolute birefringence values of MoS₂

182 with different birefringent materials, including h-BN and BaTiS₃, reported showing the highest
 183 anisotropy so far. The birefringence values for other materials in (c) were adopted from several
 184 reports.^{5–11}

185 For an unambiguous validation of the extracted dielectric function, we analyzed the planar
 186 transverse magnetic (TM) waveguide modes propagating in MoS₂ flakes employing a scattering-
 187 type scanning near-field optical microscope (s-SNOM, Methods). By recording the scattered
 188 radiation, nanoscale images corresponding to the field distribution associated with the guided
 189 mode is obtained (Figure 3a-b). The effective TM-waveguide mode index ($n_{\text{eff,TM}}$) strongly
 190 depends on the material anisotropy allowing to probe anisotropic response, in-plane (n_{ab}) and
 191 out-of-plane (n_c) refractive indices, and determined by:¹⁶

$$192 \quad \frac{2\pi d}{\lambda} \sqrt{n_{ab}^2 - n_{\text{eff,TM}}^2} \frac{n_{ab}^2}{n_c^2} = \tan^{-1} \left(\frac{n_{ab}^2}{n_{\text{Air}}^2} \frac{\sqrt{n_{\text{eff,TM}}^2 - n_{\text{Air}}^2}}{\sqrt{n_{ab}^2 - n_{\text{eff,TM}}^2} \frac{n_{ab}^2}{n_c^2}} \right) + \tan^{-1} \left(\frac{n_{ab}^2}{n_{\text{SiO}_2}^2} \frac{\sqrt{n_{\text{eff,TM}}^2 - n_{\text{SiO}_2}^2}}{\sqrt{n_{ab}^2 - n_{\text{eff,TM}}^2} \frac{n_{ab}^2}{n_c^2}} \right) + m\pi, \quad (1)$$

193 where d is the thickness of the MoS₂ flake, λ is the incident wavelength, $n_{\text{Air}} = 1$ and $n_{\text{SiO}_2} = 1.45$
 194 are air and SiO₂ refractive indices, and m is the mode order. We used incident wavelengths in the
 195 range 1470 – 1570 nm and 632.8 nm to excite guiding modes by focusing light into the apex of
 196 the s-SNOM tip, which allows for momentum matching conditions. The excited mode
 197 propagates in the MoS₂ nanoflake as cylindrical waves, which interfere with the illuminating
 198 plane wave giving rise to interferometric patterns of the near-field,²⁰ as clearly seen in Figure 3c-
 199 d. It is worth mention that while most of the previous works with s-SNOM for TMDCs focus
 200 only on the near-field amplitude,^{16,20} the most accurate results are obtained by analyzing the
 201 phase as well³⁵ (see Supporting Information for comparison). To retrieve the effective waveguide
 202 mode index, in Figure 3e, we analyzed the Fourier transform (FT) of individual line scans from
 203 Figure 3d. The resulting FT has two pronounced peaks: one around zero due to background
 204 originating mostly from a strong tip-sample coupling, and the second one associated with the
 205 planar TM-waveguide mode of interest. Note that there are no peaks in the left part of Figure 3e

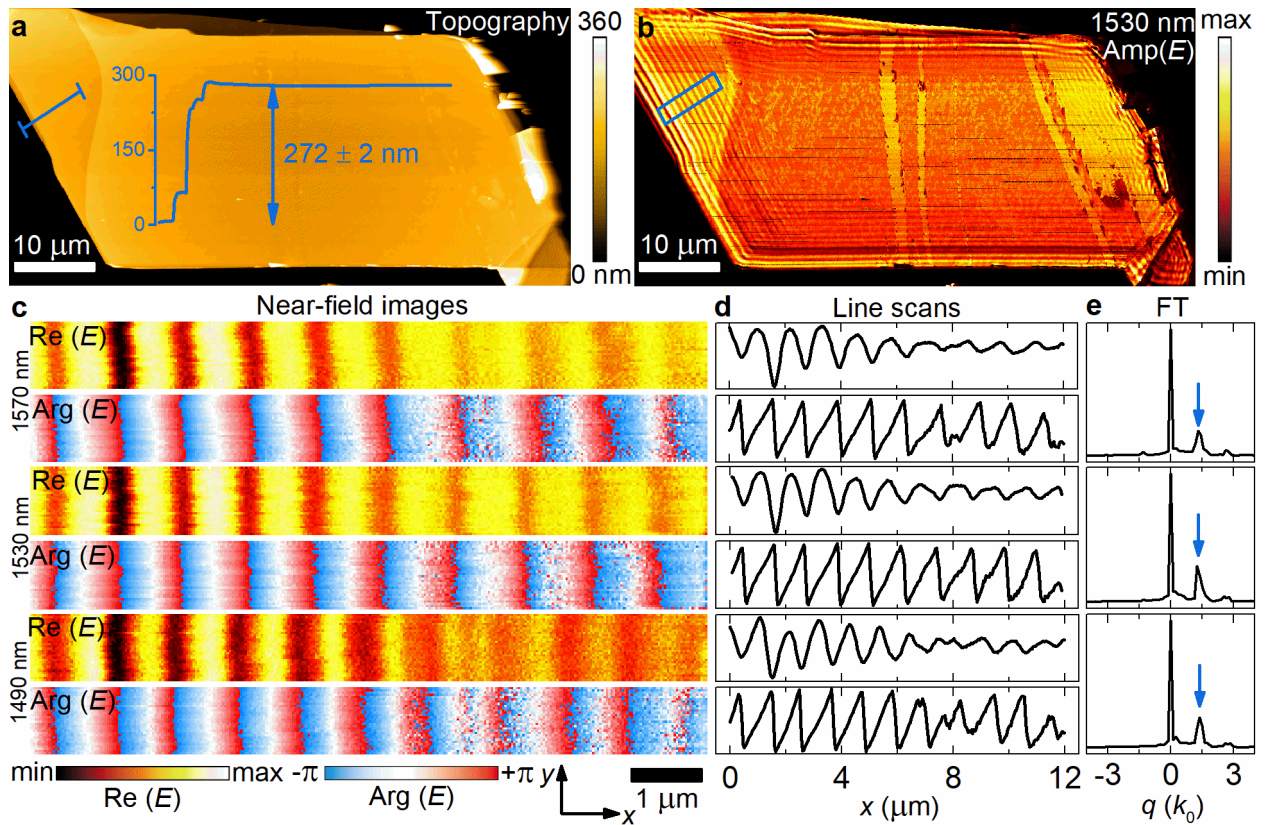
206 (for negative values of q), indicating that no modes propagate in the backward direction (from
 207 the edge to the tip). The latter implies that mode scattering by the edge is far more efficient than
 208 mode edge reflection or launching. Otherwise, we would observe standing waves with a cosine
 209 form, whose FT would be symmetrical and which are predominantly observed in nano-infrared
 210 imaging of graphene plasmons^{36,37} and hexagonal boron nitride (hBN) polaritons.³⁸ The primary
 211 reason for the observed tip-launching and edge-scattering mechanisms is the relatively small
 212 momenta of the modes²⁰ since it is much closer to the free-space photon wavevector (k_0) than in
 213 the studies of graphene^{36,37} or hBN.³⁸ For small momenta, the effective mode index is connected
 214 with that determined from the FT ($n_{s\text{-SNOM,FT}}$) by momentum conservation along the edge
 215 direction:²⁰

$$216 \quad n_{\text{eff,TM}} = n_{s\text{-SNOM,FT}} + \cos(\alpha) \cdot \sin(\beta)$$

217 (2)

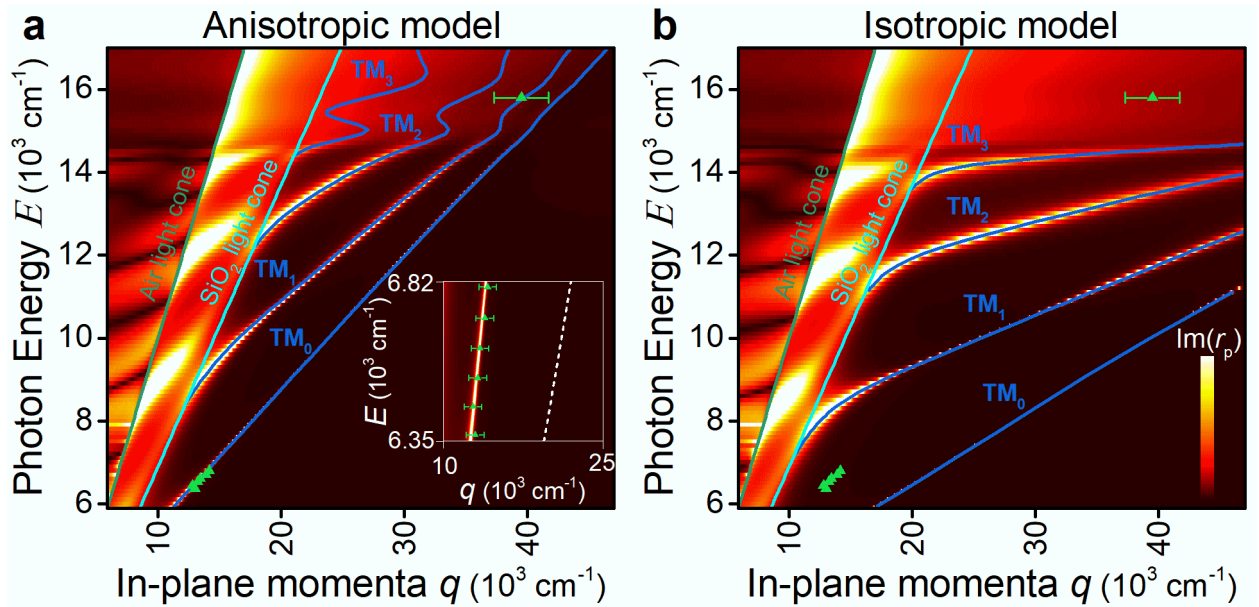
218 where in our case $\alpha = 45^\circ$ is the angle between the illumination wavevector and its projection k_{\parallel}
 219 on the sample surface plane and $\beta = 80^\circ$ is the angle between k_{\parallel} and the sample edge. Based on
 220 the extracted $n_{\text{eff,TM}}$, we constructed the energy ($E = h \cdot c / \lambda$)–momentum ($q = 1/\lambda$) dispersion
 221 relation of the waveguide mode. The obtained experimental (q, E) data points (green triangles)
 222 are overlaid on top of the calculated dispersion color map in Figure 4a using constants from
 223 Figure 2a. For reference, we also added the dispersion for an isotropic model in Figure 4b,
 224 assuming the optical constants to be the same for all crystallographic axes and equal one from
 225 ab -plane. Notably, in the visible spectral range, where excitons start playing a role, the isotropic
 226 model (Figure 4b) predicts the absence of guided modes owing to high material absorption.
 227 Conversely, our anisotropic results and near-field measurements reveal that even for this spectral
 228 interval, guided modes exist, which explains the recently discovered excitons polaritons in
 229 TMDCs.²⁰ Therefore, the excellent agreement between the experiment and theory validates our
 230 dielectric permittivity of MoS₂, allowing for predicting capabilities in future photonic devices,
 231 including polarization-maintaining fibers⁴ and polarization tunable Mie-nanoresonators for

232 nonlinear photonics³⁹ since the magnetic dipole (MD) Mie-resonance in MoS₂ nanoparticles is
 233 strongly affected by the refractive index values.⁴⁰ For instance, the spectral position of MD-
 234 resonance for a spherical particle is approximately defined by $\lambda_{\text{MD}} \approx nD$, with D being the
 235 sphere's diameter.⁴¹ Besides, its anisotropic behavior allows its use as nanoresonators even for
 236 photon energies higher than the electronic bandgap thanks to the absence of absorption along the
 237 c -axis, while for conventional isotropic materials (c-Si, GaAs, and GaSb) this option is closed.
 238 Therefore, TMDCs provide device miniaturization, and their birefringence enables fine-tuning
 239 the resonance position in a wide spectral range by altering the light polarization, which is
 240 roughly $n_{ab}D - n_cD \approx 450$ nm for a typical diameter of 300 nm.



241
 242 **Figure 3. Waveguide modes imaged by s-SNOM.** **a** Topography image of the analyzed MoS₂
 243 flake. A profile taken from the region labeled by a blue line is shown. **b** Near-field amplitude
 244 image of the flake recorded at $\lambda = 1530$ nm. The region with the strongest signal is framed by a
 245 blue rectangular. **c** Near-field images, real part $\text{Re}(E)$ and phase $\text{Arg}(E)$, of the electric field E
 246 taken at 1570 nm (top), 1530 nm (middle), and 1490 nm (bottom) in an area of the image in (b),

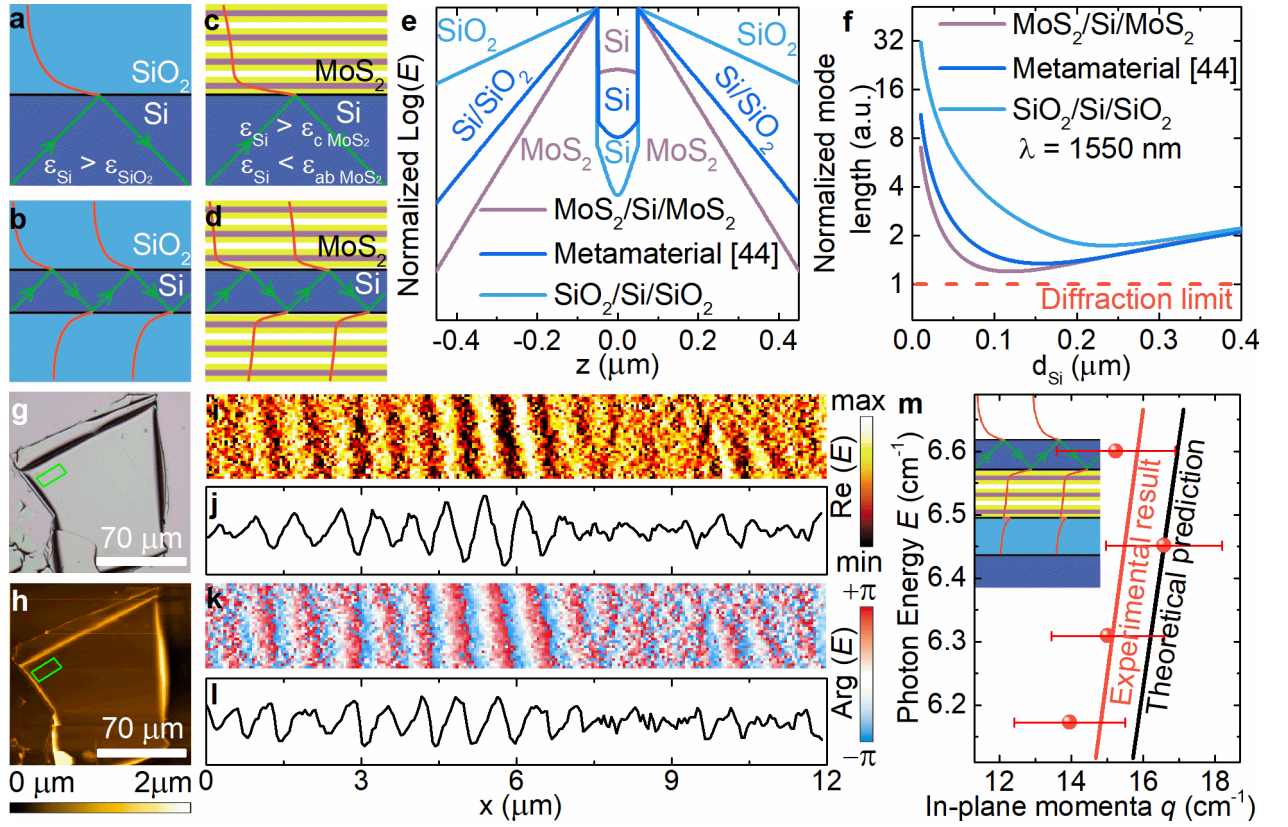
247 indicated by a blue rectangle. **d** *x*-line scans taken from **(c)** and averaged over 1.2 μm along the
 248 *y*-axis (other wavelength images are collected in Supporting Information). **e** Fourier transform
 249 (FT) amplitude of the complex near field signal in **(d)**, the blue arrow marks the peak associated
 250 with the waveguide mode.



251
 252 **Figure 4. Dispersion of a planar MoS₂ waveguide.** **a-b** Transfer matrix calculations⁴² for the
 253 MoS₂/SiO₂/Si system for anisotropic and isotropic (in the assumption of optical constants for the
 254 *c*-axis equal to those for *ab*-plane) models of MoS₂. The experimental ($q = 1/\lambda$, $E = h\cdot c/\lambda$) data
 255 points (green triangles) show good agreement with the calculated dispersion (blue lines) based
 256 on anisotropic dielectric function from Figure 2a. The inset is a magnified near-infrared spectral
 257 range with a white dashed line illustrating the isotropic case's dispersion relation.

258 More importantly, the giant anisotropy provides an avenue to resolve the fundamental
 259 limitations of isotropic materials. In this regard, extreme skin depth (e-skid) waveguide in Figure
 260 5 epitomizes the importance of highly anisotropic material as an essential building block for
 261 next-generation photonics.⁴³ This phenomenon originates from the general law of total internal
 262 reflection (TIR). In the classical case in Figure 5a, if $n_1 > n_2$ (n_1 and n_2 are the refractive indices
 263 of the medium 1 and 2) and the incident angle is greater than the critical angle, light is reflected
 264 in the first medium and decays in the second. This effect is in the core of telecommunication

265 technologies for guiding light at vast distances since light reflects without power loss. However,
266 reducing the thickness of standard (typically Si) optical waveguides down to the nanometric
267 scale introduces a big difficulty: the confinement of the electromagnetic modes in the optically
268 less dense material significantly weakens, as illustrated in Figure 5a-b and e-f. It restricts the
269 miniaturization on photonic integrated circuits because of the cross-talk (electric field
270 overlapping between adjacent waveguides).⁴⁴ To date, the best solution to the problem is the use
271 of a generalized form of TIR at the interface of isotropic and uniaxial metamaterial asserted that
272 n_1 should be larger than out-of-plane component n_c (Figure 5c).⁴⁵ Counterintuitively, the in-plane
273 component n_{ab} could have any value even higher than n_1 and, more interestingly, the greater its
274 magnitude, the better the light confinement inside the waveguide core (Figure 5d), allowing to
275 get closer to the diffraction limit ($\lambda/2n_{\text{core}}$). To experimentally demonstrate the effect, we covered
276 285 nm-thick MoS₂ flake with 190 nm-thick silicon (Methods) to form a planar e-skid
277 waveguide Air/Si/MoS₂. Although MoS₂ is better than air for light confinement, we left one of
278 the faces of the silicon slab uncovered to visualize the mode by near-field measurements shown
279 in Figure 5i-l. The waveguiding mode measured dispersion is in close agreement with the
280 theoretical calculations, thus validating the e-skid waveguide concept for light confinement and,
281 consequently, miniaturized photonic integrated circuits. It is worth mention that MoS₂ yields
282 markedly better light confinement than recently introduced metamaterial⁴³ of alternating layers
283 of Si and SiO₂ (Figure 5f) since MoS₂ is a natural metamaterial with molybdenum, sulfur and
284 vdW gap varying layers (Figure 5c-d). Finally, it leads to another concept of a vertical integrated
285 circuit, which recently has been proved to be a useful degree of freedom for efficient light
286 manipulation.⁴⁶



287

288 **Figure 5. Transparent sub-diffraction optics.** **a** Traditional total internal reflection with two
 289 isotropic media: above the critical angle, the light is reflected from the interface giving a
 290 decaying wave for a lower refractive index medium. **b** It results in long electric tails in
 291 conventional waveguides limited the current on-chip photonics. **c** Relaxed total internal
 292 reflection: the out-of-plane dielectric component is less than for isotropic material, while the
 293 high in-plane part provides substantial light compression. **d** It gives rise to a planar waveguide
 294 with outstandingly short electric tails. Red curves for **(a-d)** panels schematically shows electric
 295 field amplitude, and yellow, purple, and white colors in **(c-d)** panels label sulfur, molybdenum,
 296 and vdW gap layers. **e** Comparison of electric field distribution for MoS₂/Si/MoS₂, SiO₂/Si/SiO₂
 297 metamaterial/Si/metamaterial⁴⁵ systems reveals that giant anisotropy causes giant light
 298 compression. **f** Light confinement in MoS₂/Si/MoS₂ allows for tackling the diffraction limit
 299 compared with traditionally used SiO₂/Si/SiO₂ and recently introduced⁴⁵ metamaterial cladding
 300 with alternating layers of Si and SiO₂ using silicon as a core. **g-h** Optical image and AFM
 301 topography mapping of the flake with 190 nm covered silicon. **i-l** Near field images, real part Re
 302 (E) and phase Arg (E), with the corresponding line scans of the electric field taken at $\lambda = 1550$

303 nm from the area of (**g-h**) indicated by a green rectangular. (other wavelength images are
304 collected in Supporting Information) **m** Comparison between theoretical and experimental
305 dispersion. The inset is an artistic representation of the investigated system Air/Si (195
306 nm)/MoS₂ (285 nm)/SiO₂ (285 nm)/Si.

307

308 **DISCUSSION**

309 Optical anisotropy lies behind the functionality of many optical devices such as polarizers and
310 wave plates, to name a few. This phenomenon's outstanding importance leads to an active
311 investigation of anisotropic materials and the expansion of their application scope. However, the
312 apparatus efficiency and compactness mostly depend on absolute birefringence values, which are
313 moderate with the best result ($\Delta n < 0.8$), reported in h-BN and BaTiS₃ crystals in the visible and
314 near-infrared ranges. We believe that these limitations can be outperformed by the family of
315 TMDCs materials, whose inherent intralayer excitonic behavior results in large anisotropy along
316 and perpendicular to the layers. To validate the concept, we have shown a giant ($\Delta n > 1.5$)
317 broadband anisotropy for MoS₂ employing far and near-field techniques. Additionally, we
318 demonstrated its applicability for on-chip sub-diffraction optics. From a wider perspective, our
319 result establishes new avenues for next-generation nanophotonics based on TMDCs, for
320 example, in tunable Mie-nanoresonators, and exciton-polariton physics.

321 **ACKNOWLEDGEMENTS**

322 The authors thank Dr. Sebastian Funke, Dr. Shun Okano, Dr. Matthias Duwe, Natalia
323 Doroshina, and Valentyn Solovey for help in performing ellipsometry and Raman spectra. We
324 gratefully acknowledge financial support from the Russian Science Foundation: grants 18-19-
325 00684 (ellipsometry) and 18-79-10208 (s-SNOM). A.Y.N. acknowledges the Spanish Ministry
326 of Science, Innovation and Universities (national project no. MAT201788358-C3-3-R). P.A-G.
327 and J.D. acknowledge financial support from the European Research Council under Starting
328 Grant 715496, 2DNANOPTICA. V.G.K. and A.N.G. acknowledge EU Graphene Flagship.

329 **REFERENCES**

- 330 1. Hecht, E. *Optics* (Pearson, Harlow, 2016).
- 331 2. Weber, M. F. Giant Birefringent Optics in Multilayer Polymer Mirrors. *Science* **287**,
332 2451–2456 (2000).
- 333 3. Nicholls, L. H. *et al.* Ultrafast synthesis and switching of light polarization in nonlinear
334 anisotropic metamaterials. *Nat. Photonics* **11**, 628–633 (2017).
- 335 4. Dong, Y., Chen, L. & Bao, X. Distributed birefringence measurement of polarization
336 maintaining fiber using transient brillouin grating. *Opt. InfoBase Conf. Pap.* **35**, 193–195
337 (2010).
- 338 5. Sinton, W. M. Birefringence of Rutile in the Infrared. *J. Opt. Soc. Am.* **51**, 1309_1 (1961).
- 339 6. Ghosh, G. Dispersion-equation coefficients for the refractive index and birefringence of
340 calcite and quartz crystals. *Opt. Commun.* **163**, 95–102 (1999).
- 341 7. Zysset, B., Biaggio, I. & Günter, P. Refractive indices of orthorhombic KNbO₃ I.
342 Dispersion and temperature dependence. *J. Opt. Soc. Am. B* **9**, 380 (1992).
- 343 8. Zelmon, D. E., Small, D. L. & Jundt, D. Infrared corrected Sellmeier coefficients for
344 congruently grown lithium niobate and 5 mol% magnesium oxide –doped lithium niobate.
345 *J. Opt. Soc. Am. B* **14**, 3319 (1997).
- 346 9. Boyd, G. D., Kasper, H. & McFee, J. H. Linear and Nonlinear Optical Properties of
347 AgGaS₂, CuGaS₂, and CuInS₂, and Theory of the Wedge Technique for the Measurement
348 of Nonlinear Coefficients. *IEEE J. Quantum Electron.* **7**, 563–573 (1971).
- 349 10. Niu, S. *et al.* Giant optical anisotropy in a quasi-one-dimensional crystal. *Nat. Photonics*
350 **12**, 392–396 (2018).
- 351 11. Segura, A. *et al.* Natural optical anisotropy of h-BN: Highest giant birefringence in a bulk
352 crystal through the mid-infrared to ultraviolet range. *Phys. Rev. Mater.* **2**, 1–6 (2018).
- 353 12. Álvarez-Pérez, G. *et al.* Infrared Permittivity of the Biaxial van der Waals Semiconductor
354 α -MoO₃ from Near- and Far-Field Correlative Studies. *Adv. Mater.* **32**, 1908176 (2020).
- 355 13. Taboada-Gutiérrez, J. *et al.* Broad spectral tuning of ultra-low-loss polaritons in a van der
356 Waals crystal by intercalation. *Nat. Mater.* **19**, 964–968 (2020)
- 357 14. Kats, M. A. *et al.* Giant birefringence in optical antenna arrays with widely tailorable
358 optical anisotropy. *Proc. Natl. Acad. Sci. U. S. A.* **109**, 12364–12368 (2012).
- 359 15. Rasamani, K. D., Alimohammadi, F. & Sun, Y. Interlayer-expanded MoS₂. *Mater. Today*
360 **20**, 83–91 (2017).
- 361 16. Hu, D. *et al.* Probing optical anisotropy of nanometer-thin van der waals microcrystals by
362 near-field imaging. *Nat. Commun.* **8**, 1471 (2017).
- 363 17. Liang, W. Y. Reflection spectra of molybdenum disulphide crystals. *Phys. Lett. A* **24**,
364 573–574 (1967).
- 365 18. Hu, F. & Fei, Z. Recent Progress on Exciton Polaritons in Layered Transition-Metal
366 Dichalcogenides. *Adv. Opt. Mater.* **1901003**, 1–16 (2019).
- 367 19. Mupparapu, R., Bucher, T. & Staude, I. Integration of two-dimensional transition metal
368 dichalcogenides with Mie-resonant dielectric nanostructures. *Adv. Phys. X* **5**, 1734083
369 (2020).

- 370 20. Hu, F. *et al.* Imaging exciton-polariton transport in MoSe₂ waveguides. *Nat. Photonics* **11**,
371 356–360 (2017).
- 372 21. Babicheva, V. E. *et al.* Near-Field Surface Waves in Few-Layer MoS₂. *ACS Photonics* **5**,
373 2106–2112 (2018).
- 374 22. Hu, D. *et al.* Tunable Modal Birefringence in a Low-Loss Van Der Waals Waveguide.
375 *Adv. Mater.* **31**, 1807788 (2019).
- 376 23. Verre, R. *et al.* Transition metal dichalcogenide nanodisks as high-index dielectric Mie
377 nanoresonators. *Nat. Nanotechnol.* **14**, 679–684 (2019).
- 378 24. Guo, Y. *et al.* Probing the Dynamics of the Metallic-to-Semiconducting Structural Phase
379 Transformation in MoS₂ Crystals. *Nano Lett.* **15**, 5081–5088 (2015).
- 380 25. Gong, Z. *et al.* Magnetoelectric effects and valley-controlled spin quantum gates in
381 transition metal dichalcogenide bilayers. *Nat. Commun.* **4**, 1–6 (2013).
- 382 26. Das, S., Gupta, G. & Majumdar, K. Layer degree of freedom for excitons in transition
383 metal dichalcogenides. *Phys. Rev. B* **99**, 165411 (2019).
- 384 27. Ermolaev, G. A. *et al.* Broadband optical properties of monolayer and bulk MoS₂. *npj 2D*
385 *Mater. Appl.* **4**, 1–6 (2020).
- 386 28. Kozawa, D. *et al.* Photocarrier relaxation pathway in two-dimensional semiconducting
387 transition metal dichalcogenides. *Nat. Commun.* **5**, 1–7 (2014).
- 388 29. Ermolaev, G. A., Yakubovsky, D. I., Stebunov, Y. V., Arsenin, A. V. & Volkov, V. S.
389 Spectral ellipsometry of monolayer transition metal dichalcogenides: Analysis of
390 excitonic peaks in dispersion. *J. Vac. Sci. Technol. B* **38**, 014002 (2020).
- 391 30. Baranov, D. G. *et al.* All-dielectric nanophotonics: the quest for better materials and
392 fabrication techniques. *Optica* **4**, 814 (2017).
- 393 31. Herzinger, C. M., Johs, B., McGahan, W. A., Woollam, J. A. & Paulson, W. Ellipsometric
394 determination of optical constants for silicon and thermally grown silicon dioxide via a
395 multi-sample, multi-wavelength, multi-angle investigation. *J. Appl. Phys.* **83**, 3323–3336
396 (1998).
- 397 32. Jellison, G. E. Optical functions of GaAs, GaP, and Ge determined by two-channel
398 polarization modulation ellipsometry. *Opt. Mater. (Amst.)* **1**, 151–160 (1992).
- 399 33. Ferrini, R., Patrini, M. & Franchi, S. Optical functions from 0.02 to 6 eV of
400 Al_xGa_{1-x}Sb/GaSb epitaxial layers. *J. Appl. Phys.* **84**, 4517–4524 (1998).
- 401 34. Wilson, J. A. & Yoffe, A. D. The transition metal dichalcogenides discussion and
402 interpretation of the observed optical, electrical and structural properties. *Adv. Phys.* **18**,
403 193–335 (1969).
- 404 35. DeVault, C. T. *et al.* Suppression of near-field coupling in plasmonic antennas on epsilon-
405 near-zero substrates. *Optica* **5**, 1557 (2018).
- 406 36. Fei, Z. *et al.* Gate-tuning of graphene plasmons revealed by infrared nano-imaging.
407 *Nature* **486**, 82–85 (2012).
- 408 37. Chen, J. *et al.* Optical nano-imaging of gate-tunable graphene plasmons. *Nature* **487**, 77–
409 81 (2012).
- 410 38. Dai, S. *et al.* Tunable Phonon Polaritons in Atomically Thin van der Waals Crystals of
411 Boron Nitride. *Science* **343**, 1125–1129 (2014).

- 412 39. Koshelev, K. *et al.* Subwavelength dielectric resonators for nonlinear nanophotonics.
413 *Science* **367**, 288–292 (2020).
- 414 40. Evlyukhin, A. B. *et al.* Demonstration of magnetic dipole resonances of dielectric
415 nanospheres in the visible region. *Nano Lett.* **12**, 3749–3755 (2012).
- 416 41. Kuznetsov, A. I., Miroshnichenko, A. E., Fu, Y. H., Zhang, J. & Lukyanchukl, B.
417 Magnetic light. *Sci. Rep.* **2**, 1–6 (2012).
- 418 42. Passler, N. C. & Paarmann, A. Generalized 4×4 matrix formalism for light propagation
419 in anisotropic stratified media: study of surface phonon polaritons in polar dielectric
420 heterostructures. *J. Opt. Soc. Am. B* **34**, 2128 (2017).
- 421 43. Jahani, S. & Jacob, Z. Transparent subdiffraction optics: nanoscale light confinement
422 without metal. *Optica* **1**, 96 (2014).
- 423 44. Lukas Chrostowski. *Silicon Photonics Design: From Device to System*. (Cambridge
424 University Press, Cambridge, 2010).
- 425 45. Jahani, S. *et al.* Controlling evanescent waves using silicon photonic all-dielectric
426 metamaterials for dense integration. *Nat. Commun.* **9**, (2018).
- 427 46. Voronin, K. V., Stebunov, Y. V., Voronov, A. A., Arsenin, A. V. & Volkov, V. S.
428 Vertically coupled plasmonic racetrack ring resonator for biosensor applications. *Sensors*
429 **20**, 1–11 (2020).

430 **METHODS**

431 **Sample preparation.** The MoS₂ microcrystals were exfoliated on silicon wafers with 285-nm-
432 thick thermal SiO₂ from a synthetically grown bulk MoS₂ sample purchased from the 2D
433 Semiconductors Inc.

434 **Ellipsometry setup.** Imaging spectroscopic ellipsometry (ISE) measurements were performed
435 with a commercial spectroscopic nulling ellipsometer EP4 (<https://accurion.com>). Spectroscopic
436 data are obtained in the spectral range 360 – 1700 nm in step with 1 nm. The light is guided
437 through for linear polarization and then through a compensator to prepare elliptically polarized
438 collimated light so that the reflected light from the sample is again linearly polarized. The
439 reflected light is directed through a 10x objective to a CCD camera (microscope configuration).
440 In a suitable coordinate system, the complex reflectance matrix is described by $\tan(\Psi) \cdot \exp(i\Delta)$.
441 The analytical Ψ and Δ are calculated using Fresnel formulas.¹

442 **Near-field optical nano-spectroscopy.** The nano-imaging recording was performed using a
443 commercial s-SNOM (www.neaspec.com). The s-SNOM is based on a tapping-mode AFM
444 illuminated by a monochromatic tunable laser of the wavelength from 1470 – 1570 nm spectral

445 interval or He-Ne laser with the wavelength 632.8 nm. The near-field images were registered by
446 pseudo-heterodyne interferometric module with tip-tapping frequency around 270 kHz with an
447 amplitude of about 40 nm. The noise was significantly suppressed by demodulating the optical
448 signal with a pseudo-heterodyne interferometer at high harmonics, $n\Omega$ (in our case third
449 harmonics).

450 **Raman spectroscopy.** The experimental setup used for Raman measurements was a confocal
451 scanning Raman microscope Horiba LabRAM HR Evolution (<https://www.horiba.com/>). The
452 measurements were carried out using linearly polarized excitation at a wavelengths of 532 and
453 632.8 nm, 300 lines/mm diffraction grating, and $\times 100$ objective (N.A. = 0.90), whereas we used
454 unpolarized detection to have a significant signal-to-noise ratio. The spot size was $\sim 0.43 \mu\text{m}$.
455 The Raman spectra were recorded with 0.26 mW incident powers and an integration time of 10
456 s.

457 **First-principle calculations.** Optical properties of 2H-MoS₂ were calculated using density
458 functional theory (DFT) within the generalized gradient approximation⁴⁶ (Perdew-Burke-
459 Ernzerhof functional) and the projector-augmented wave (PAW) method⁴⁷ as implemented in the
460 Vienna Ab initio Simulation Package (VASP).⁴⁸ A two-step approach was used: first, MoS₂
461 crystal structure was relaxed, and a one-electron basis set was obtained from a standard DFT
462 calculation; second, micro- and macroscopic dielectric tensors were calculated using GW
463 approximation. Plane wave kinetic energy cutoff was set to 400 eV, and the Γ -centered k-points
464 mesh sampled the Brillouin zone with a resolution of $2\pi \cdot 0.05 \text{ \AA}^{-1}$.

465 REFERENCES

- 466 47. Perdew, J.P., Burke, K. & Ernzerhof, M. Generalized Gradient Approximation Made
467 Simple. *Phys. Rev. Lett.* **77**, 3865–3868 (1996).
- 468 48. Kresse, G. & Joubert, D. From ultrasoft pseudopotentials to the projector augmented-
469 wave method. *Phys. Rev. B* **59**, 1758–1775 (1999).

470 49. Kresse, G. & Furthmüller, J. Efficiency of ab-initio total energy calculations for metals
471 and semiconductors using a plane-wave basis set. *Computational Materials Science* **6**,
472 15–50 (1996).

Figures

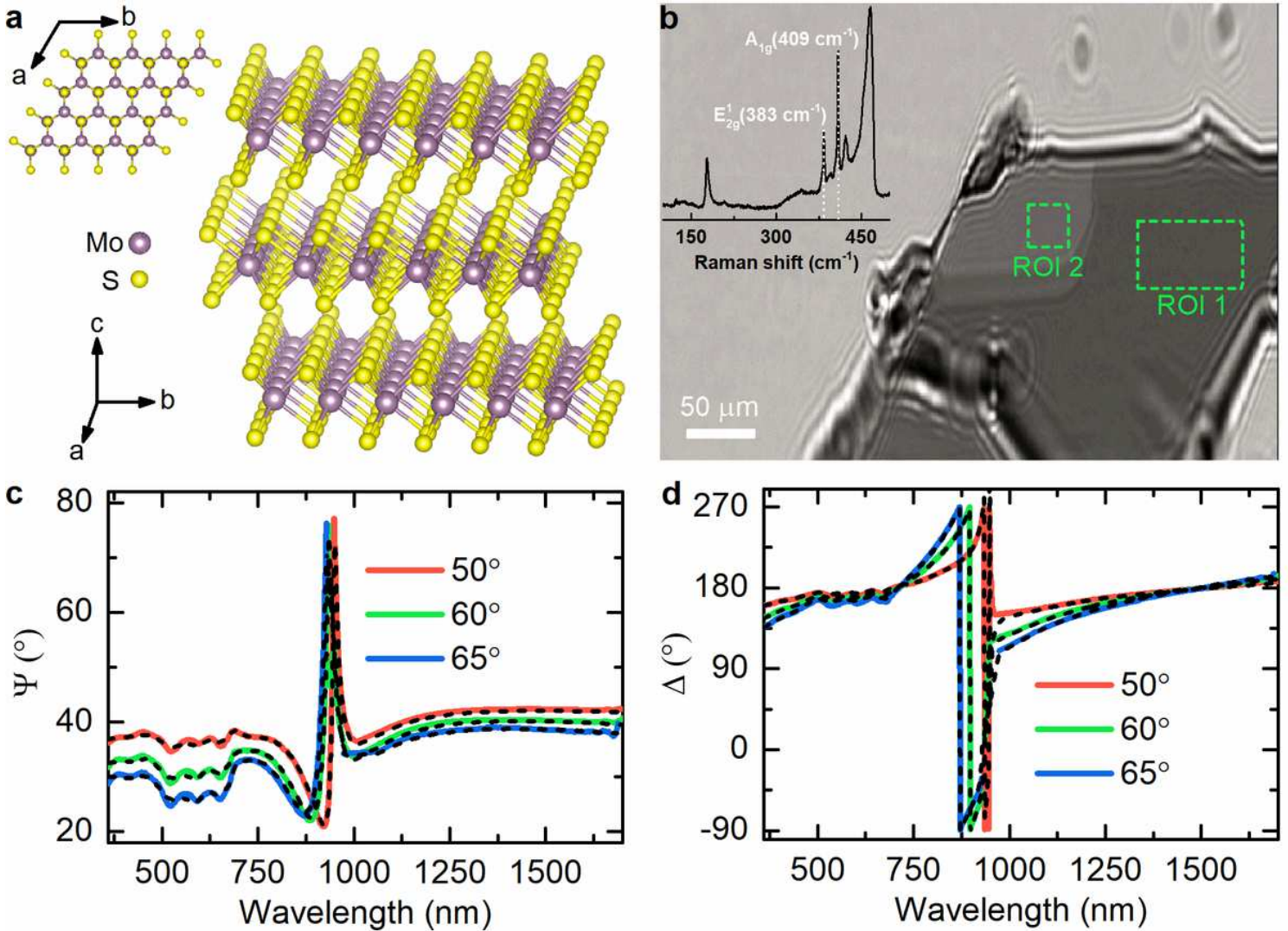


Figure 1

Anisotropy in MoS₂. a Schematic illustration of the MoS₂ layered structure: the giant anisotropy between ab-plane and c-axis arises from different interlayer (weak van der Waals bonding) and intralayer (strong ionic/covalent bonding) atomic interactions. b Optical ellipsometry microscope image of the exfoliated MoS₂ thin film on a 285 nm-thick SiO₂/Si substrate at 65°. The ellipsometry measurements were performed in the two uniform areas marked by the green dashed lines. The inset shows a resonant Raman spectrum at an excitation wavelength $\lambda = 632.8$ nm with the characteristic modes $E_{2g}^1 = 383$ cm⁻¹ and $A_{1g} = 409$ cm⁻¹, whose positions confirm the 2H semiconducting material configuration. c-d Experimental (solid lines) and analytically calculated (dashed lines, see Methods) ellipsometric parameters Ψ and Δ for ROI 1 (Ψ and Δ for ROI 2 see in Supporting Information) at three incident angles 50°, 60°, and 65°. The asymmetric interference-like peak at around 900 nm is induced by interference enhancement in SiO₂ caused by splitting the incident beam into ordinary and extraordinary beams indicating a giant anisotropy in MoS₂.

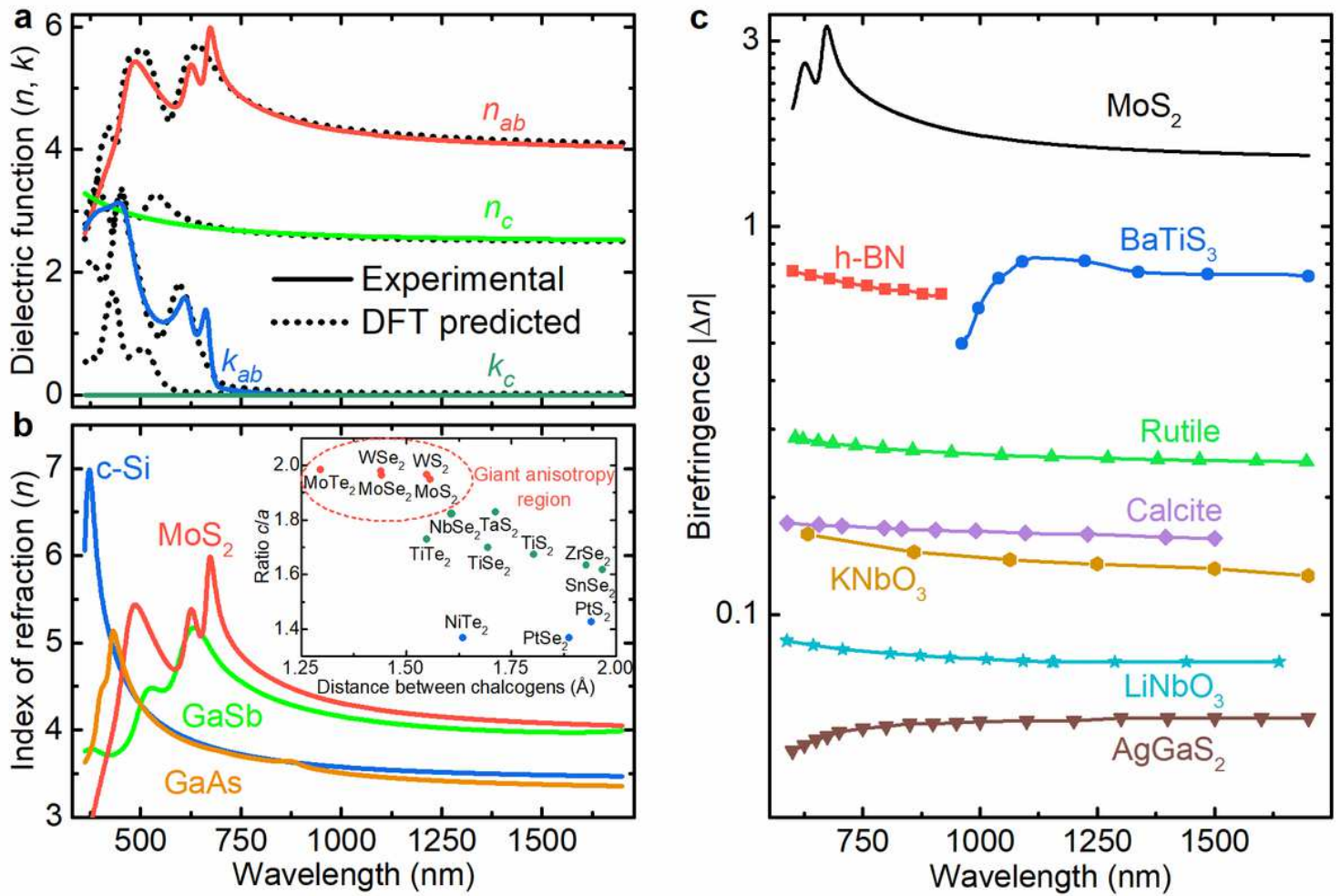


Figure 2

Optical anisotropy of MoS₂. a Real (n) and imaginary (k) parts of the dielectric function along the ab-plane and c-axis. b Comparison of the MoS₂ refractive index along the ab-plane with other high-refractive-index materials commonly used in nanophotonics.^{31–33} The inset compares the ratio of crystal parameters (c and a in Figure 1a) versus distance between neighboring chalcogens (S, Se, and Te) for various TMDCs. The highest anisotropy is expected for TMDCs denoted by red circles, while the lowest for blue. The crystallographic data were adopted from the review article.³⁴ c Comparison of the absolute birefringence values of MoS₂ with different birefringent materials, including h-BN and BaTiS₃, reported showing the highest anisotropy so far. The birefringence values for other materials in (c) were adopted from several reports.^{5–11}

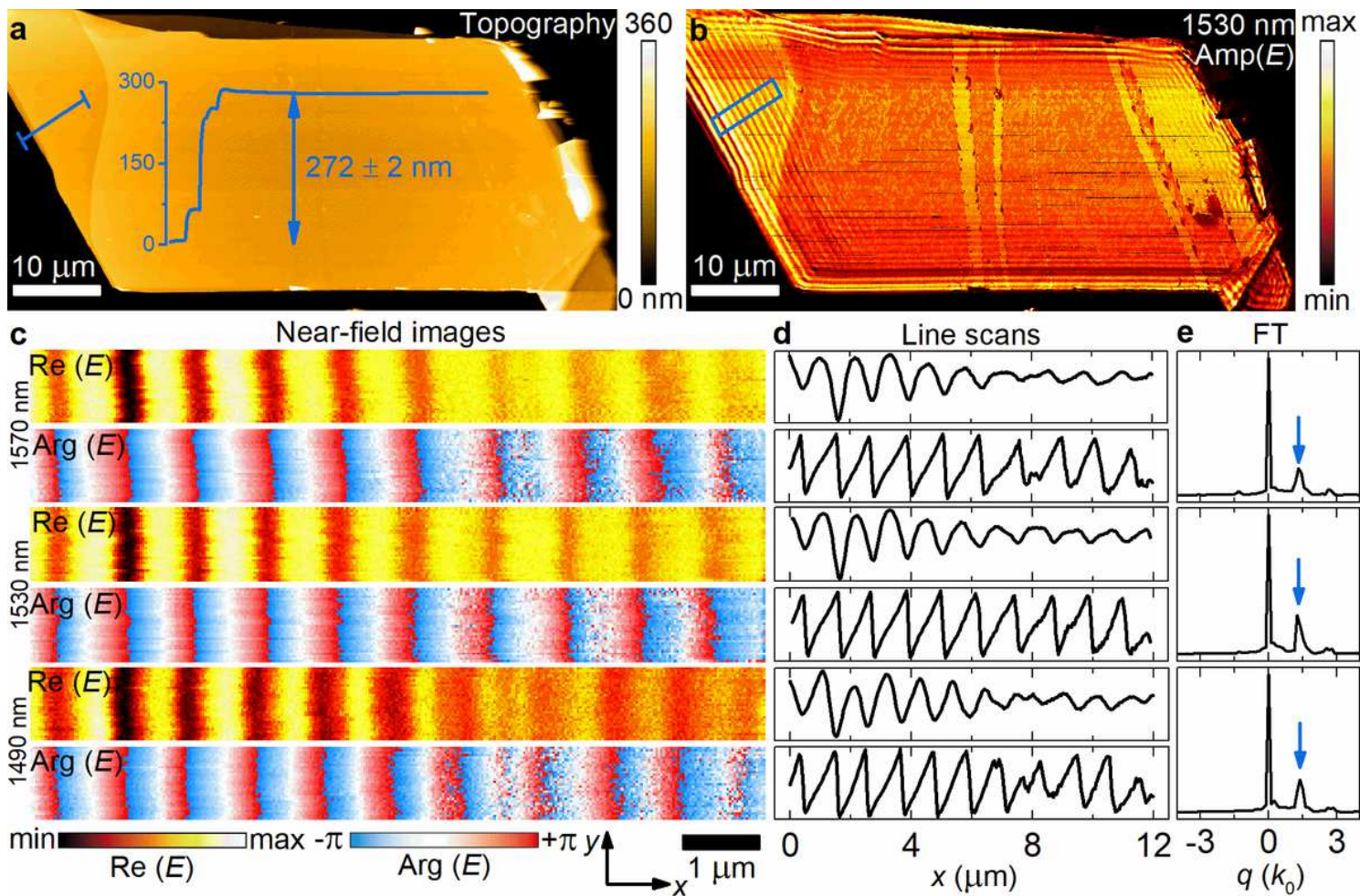


Figure 3

Waveguide modes imaged by s-SNOM. a Topography image of the analyzed MoS₂ flake. A profile taken from the region labeled by a blue line is shown. b Near-field amplitude image of the flake recorded at $\lambda = 1530$ nm. The region with the strongest signal is framed by a blue rectangular. c Near-field images, real part $\text{Re}(E)$ and phase $\text{Arg}(E)$, of the electric field E taken at 1570 nm (top), 1530 nm (middle), and 1490 nm (bottom) in an area of the image in (b), indicated by a blue rectangle. d x-line scans taken from (c) and averaged over $1.2 \mu\text{m}$ along the y-axis (other wavelength images are collected in Supporting Information). e Fourier transform (FT) amplitude of the complex near field signal in (d), the blue arrow marks the peak associated with the waveguide mode.

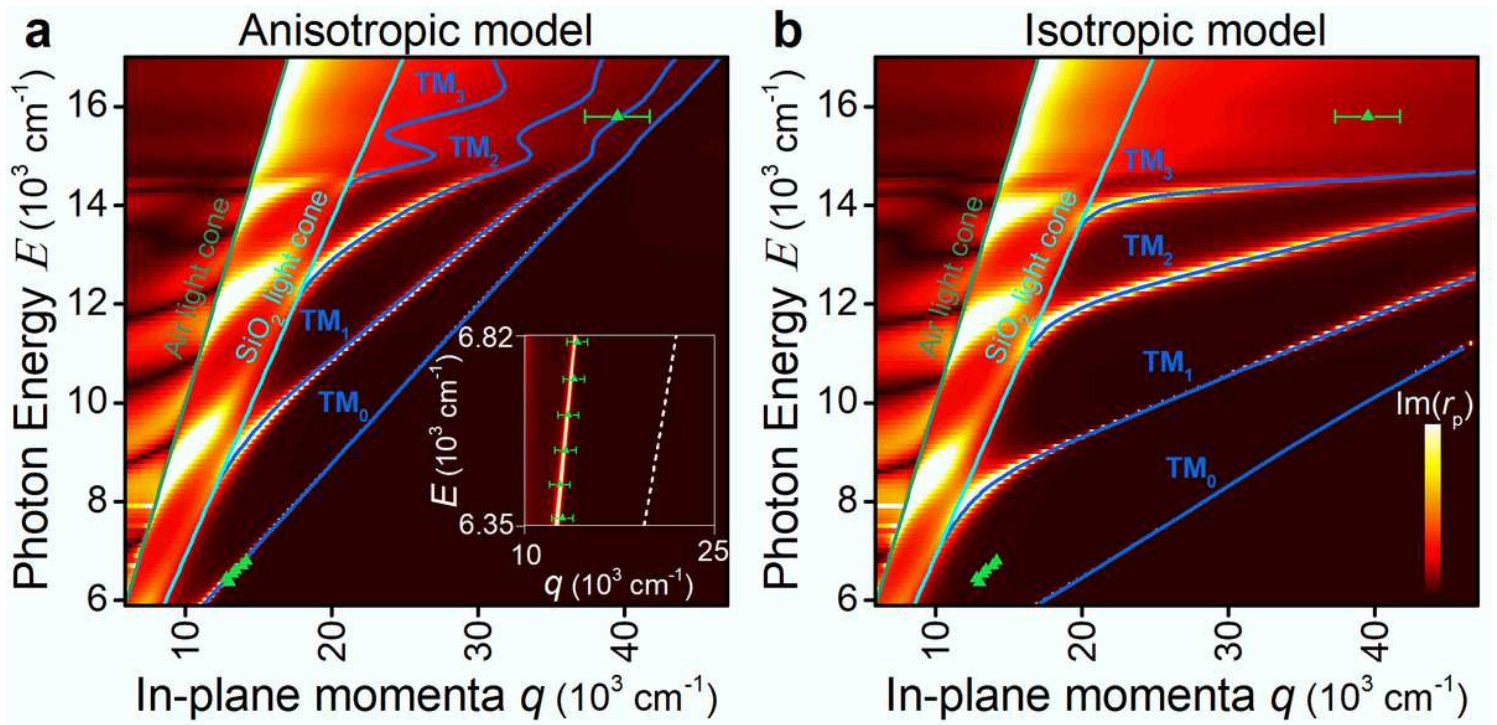


Figure 4

Dispersion of a planar MoS₂ waveguide. a-b Transfer matrix calculations⁴² for the MoS₂/SiO₂/Si system for anisotropic and isotropic (in the assumption of optical constants for the c-axis equal to those for ab-plane) models of MoS₂. The experimental ($q = 1/\lambda$, $E = h\nu/c/\lambda$) data points (green triangles) show good agreement with the calculated dispersion (blue lines) based on anisotropic dielectric function from Figure 2a. The inset is a magnified near-infrared spectral range with a white dashed line illustrating the isotropic case's dispersion relation.

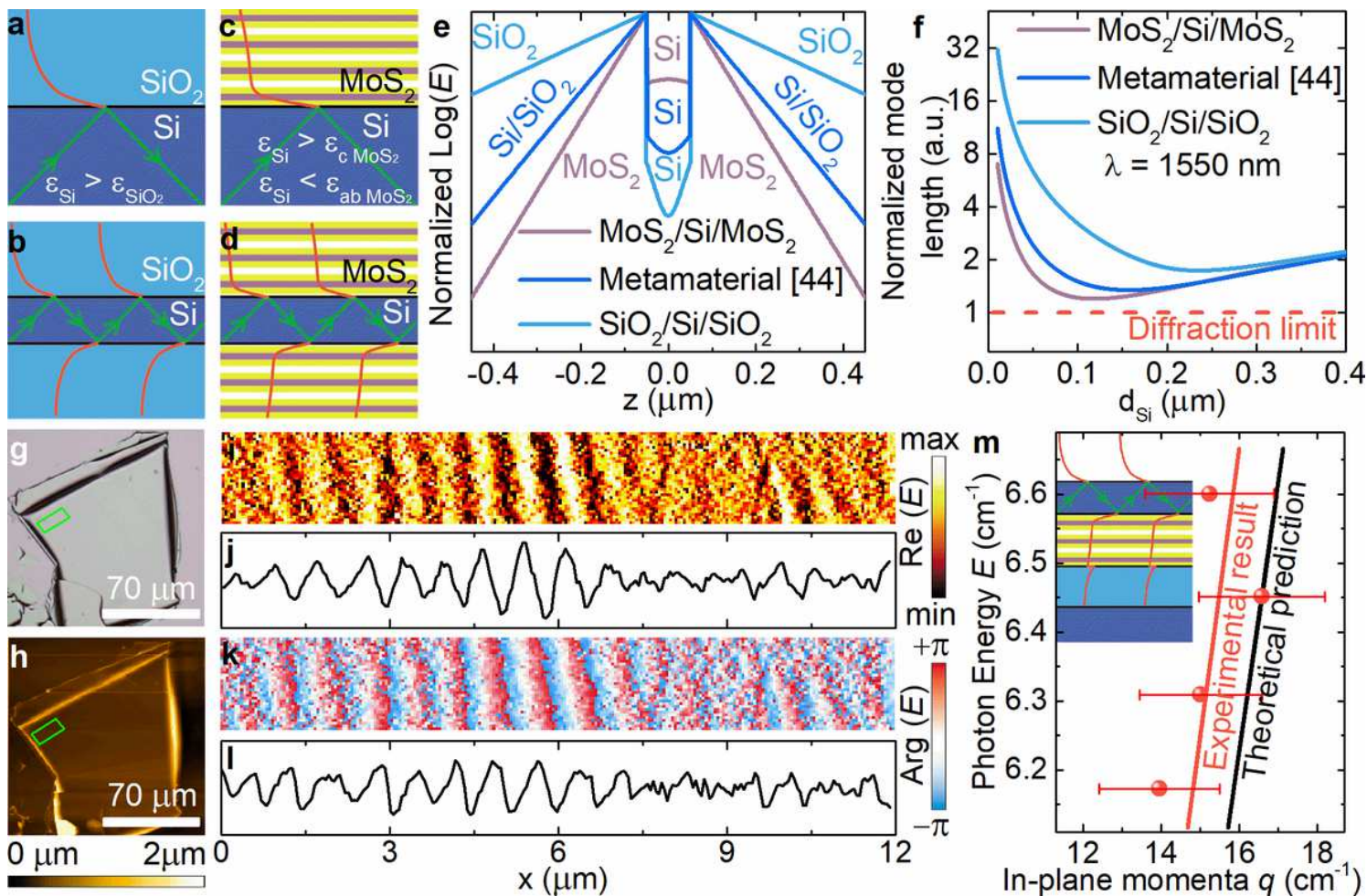


Figure 5

Transparent sub-diffraction optics. a Traditional total internal reflection with two isotropic media: above the critical angle, the light is reflected from the interface giving a decaying wave for a lower refractive index medium. b It results in long electric tails in conventional waveguides limited the current on-chip photonics. c Relaxed total internal reflection: the out-of-plane dielectric component is less than for isotropic material, while the high in-plane part provides substantial light compression. d It gives rise to a planar waveguide with outstandingly short electric tails. Red curves for (a-d) panels schematically shows electric field amplitude, and yellow, purple, and white colors in (c-d) panels label sulfur, molybdenum, and vdW gap layers. e Comparison of electric field distribution for MoS₂/Si/MoS₂, SiO₂/Si/SiO₂ metamaterial/Si/metamaterial⁴⁵ systems reveals that giant anisotropy causes giant light compression. f Light confinement in MoS₂/Si/MoS₂ allows for tackling the diffraction limit compared with traditionally used SiO₂/Si/SiO₂ and recently introduced⁴⁵ metamaterial cladding with alternating layers of Si and SiO₂ using silicon as a core. g-h Optical image and AFM topography mapping of the flake with 190 nm covered silicon. i-l Near field images, real part Re (E) and phase Arg (E), with the corresponding line scans of the electric field taken at λ = 1550 nm from the area of (g-h) indicated by a green rectangular. (other wavelength images are collected in Supporting Information) m Comparison between theoretical and experimental dispersion. The inset is an artistic representation of the investigated system Air/Si (195 nm)/MoS₂ (285 nm)/SiO₂ (285 nm)/Si.

Supplementary Files

This is a list of supplementary files associated with this preprint. Click to download.

- [GiantanisotropyinthinMoS2filmsSirevisedv3.docx](#)